Biophysical Journal
Article

Biophysical Society

Modulation of Toroidal Proteins Dynamics in Favor of Functional Mechanisms upon Ligand Binding

Hongchun Li,[1,2,3] Pemra Doruker,[2] Guang Hu,[1,*] and Ivet Bahar[2,*]
[1]Center for Systems Biology, School of Biology and Basic Medical Sciences, Soochow University, Suzhou, China; [2]Department of Computational and Systems Biology, School of Medicine, University of Pittsburgh, Pittsburgh, Pennsylvania; and [3]Research Center for Computer-Aided Drug Discovery, Shenzhen Institutes of Advanced Technology, Chinese Academy of Sciences, Shenzhen, China

ABSTRACT Toroidal proteins serve as molecular machines and play crucial roles in biological processes such as DNA replication and RNA transcription. Despite progress in the structural characterization of several toroidal proteins, we still lack a mechanistic understanding of the significance of their architecture, oligomerization states, and intermolecular interactions in defining their biological function. In this work, we analyze the collective dynamics of toroidal proteins with different oligomerization states, namely, dimeric and trimeric DNA sliding clamps, nucleocapsid proteins (4-, 5-, and 6-mers) and Trp RNA-binding attenuation proteins (11- and 12-mers). We observe common global modes, among which cooperative rolling stands out as a mechanism enabling DNA processivity, and clamshell motions as those underlying the opening/closure of the sliding clamps. Alterations in global dynamics due to complexation with DNA or the clamp loader are shown to assist in enhancing motions to enable robust function. The analysis provides new insights into the differentiation and enhancement of functional motions upon intersubunit and intermolecular interactions.

SIGNIFICANCE Our study provides new insights into the topology-dynamics-function relationships of toroidal proteins, which underlie their design and machinery. We note that a global rolling movement of torus enables the sliding of β-clamp with respect to double-stranded DNA, whereas clamshell-like movements facilitate clamp opening/closure in close agreement with the structural transition experimentally observed in the bacteriophage T4 clamp. We provide a comprehensive classification of the collective modes based on diverse toroidal systems and show how they are modulated upon binding of substrates, including clamp loader and DNA/RNA. We also observe that the naturally abundant oligomers of nucleocapsid proteins and Trp RNA-binding attenuation proteins exhibit the tightest interfaces with the highest mechanical stiffness among their family members with different oligomerization states, consistent with their resistance to destabilization.

INTRODUCTION

Toroidal topology is commonly observed in biomolecular machines associated with DNA and RNA binding and processing (1–3), such as sliding clamps, helicases, and Lsm proteins. Toroidal proteins are made up of two or more subunits. Subunits in toroidal oligomers share the same type of interfacial interactions because of homo-oligomerization (4). As such, they form an excellent platform for investigating the role of protein-protein associations and subunit fold/topology in driving functional dynamics (5).

Fig. 1 displays three common types of DNA-/RNA-binding proteins, which will form the basis of this study. The first type encompasses the dimeric and trimeric sliding clamps (respective Fig. 1, *a* and *b*) that increase the processivity of DNA polymerases during DNA synthesis. The clamps encircle, and slide along, the double-stranded DNA (dsDNA), and at the same time, they stay bound to the polymerase so that it can perform continuous replication. The first clamp structure, β-clamp polymerase processivity factor determined for *Escherichia coli* DNA polymerase III (6), has two β-subunits, each composed of three domains with identical folds. Thus, it displays a sixfold symmetry, where 12 α-helices and 6 β-sheets shape the inner and outer surfaces of the torus, respectively. This β-clamp (designated as clamp-2) in complex with dsDNA (7) is shown in Fig. 1 *a*. DNA polymerase δ processivity factor proliferating cell

Submitted August 29, 2019, and accepted for publication January 27, 2020.
*Correspondence: huguang@suda.edu.cn or bahar@pitt.edu
Hongchun Li and Pemra Doruker contributed equally to this work.
Editor: Wilma Olson.
https://doi.org/10.1016/j.bpj.2020.01.046

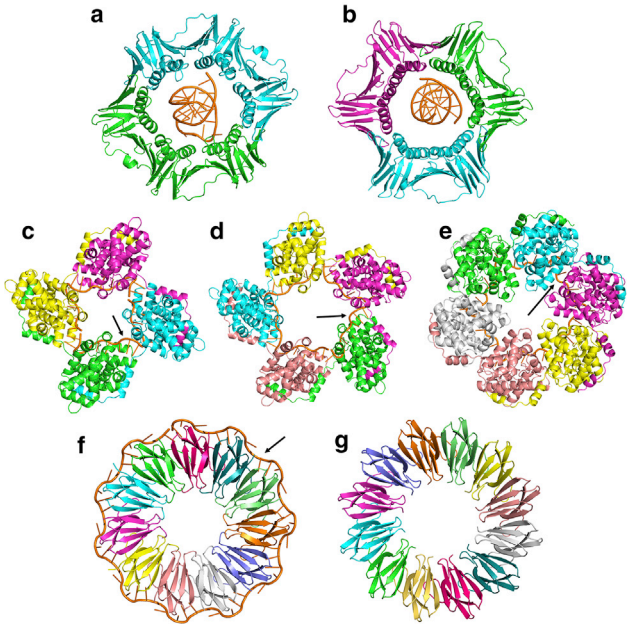

FIGURE 1 X-ray structure of toroidal proteins with different oligomerization states. (*a*) Dimeric clamp structure (PDB: 3BEP) of the β-clamp polymerase processivity factor from *E. coli* is shown. (*b*) Trimeric clamp (PDB: 6GIS) of human DNA polymerase δ processivity factor PCNA is shown. (*c–e*) Nucleocapsid protein (NCP) from Rift Valley fever (RVF) virus in tetrameric (PDB: 4H5P) (*c*), pentameric (PDB: 4H5O) (*d*), and hexameric (PDB: 4V9E) (*e*) states is shown. (*f*) Undecameric (PDB: 1C9S) and (*g*) dodecameric (PDB: 2EXT) TRAP (Trp RNA-binding attenuation protein) from *G. stearothermophilus* is shown. Subunits are shown in different colors. The bound dsDNA or ssRNA are rendered in orange stick representation (in *a–f*). Black arrows in (*c*)–(*f*) point to an example ssRNA molecule in each structure. To see this figure in color, go online.

nuclear antigen (PCNA) is another clamp, which is a trimer of two-domain subunits, similarly with sixfold symmetry. Fig. 1 *b* displays the human PCNA (also known as clamp-3) sliding clamp complexed with DNA (8,9).

Nucleocapsid proteins (NCPs) from Rift Valley fever (RVF) and Toscana viruses assemble into tori (10,11) in either free or oligomeric RNA-bound form. A highly flexible α-helical arm mediates the interactions of each NCP subunit with the neighboring subunit, leading to tetrameric (NCP-4, Fig. 1 *c*), pentameric (NCP-5, Fig. 1 *d*) and the most commonly observed hexameric (NCP-6, Fig. 1 *e*) states. Single-stranded viral RNA (ssRNA) bases are sequestered by nonspecific binding in a narrow, continuous groove lining the inner surface of the torus (11). This mode of NCP-RNA binding is highly accommodating for toroidal topologies as well as nonsymmetric, extended structures identified in the electron micrograph of the RVF virus (11,12).

The third toroidal structure is from the Trp RNA-binding attenuation protein (TRAP). The wild-type TRAP forms an 11-subunit torus (13), which in the presence of Trp binds to a 53-base-long RNA wrapping around the ring (TRAP-11, Fig. 1 *f*). A TRAP composed of 12 subunits (TRAP-12, Fig. 1 *g*) has been engineered by removing five C-terminal residues at the outer side of the intersubunit axis from the wild-type dodecamer (14).

Molecular dynamics simulations and/or studies based on elastic network models (ENMs) have been utilized to study the conformational dynamics of sliding clamps (15–17) and TRAPs (18,19), the interactions of dsDNA with PCNA (20) and ssRNA with TRAP (21), and the interfacial properties of the β-clamp (22–24). Nuclear pore complex collective modes have been identified by ENMs in comparison to tori with uniform and varying mass distribution (25). However, the global modes that are commonly shared by toroidal proteins and their modifications caused by ligand binding have not been characterized so far. Although simulations/analyses of individual proteins provide information on their dynamics case by case, recent work has demonstrated that a systematic analysis of families of proteins sharing similar folds provides deeper insights into their signature dynamics and differentiation among family members (26–28). Another important aspect of functional speciation is the role of complexation and oligomerization in acquiring or modifying molecular mechanisms of motions that lend themselves to biological function. Yet, current full atomic models and simulations do not allow for a comparative study of multimeric protein dynamics because of time and memory limitations. Instead, we conduct in this study an extensive ENM analysis of the conformational dynamics of RNA-/DNA-binding proteins, in RNA-/DNA-bound and -free forms, with diverse oligomerization states and toroidal shapes. We utilize ENMs because of their efficiencies in determining the collective motions and conformational changes of large structures/assemblies governed by the multimeric protein shape/topology (29–37) while also providing an accurate sampling of the conformational space, as demonstrated by extensive comparisons with ensembles of known structures (resolved for a given protein, including HIV-1 reverse transcriptase) and implemented in ProDy (38,39). Numerous studies have shown that ENM-generated global modes of motion are in good agreement with the principal modes of structural changes deduced from principal component analysis of such ensembles of structures (38–41). Furthermore, ENM-sampled softest (lowest frequency, highly cooperative) motions have been shown to agree well with the essential modes sampled in molecular dynamics simulations, provided that these simulations are long enough or complemented by advanced sampling algorithms (42–44).

This study provides insights into the structural basis of functional modes that aid clamp processivity, namely, clamp sliding and opening/closing. ENMs have also been broadly used for identifying the interfacial dynamics and allosteric features of protein complexes and oligomers (45–51). Along this line, we will focus on the changes in subunit dynamics upon complexation with oligonucleotides and the mechanistic aspects of subunit interfaces in different oligomeric states in relation to functional interactions with DNA and

RNA molecules. Our study will show how the intrinsically accessible motions uniquely encoded by the toroidal architecture and oligomerization state are used for enabling or enhancing the mechanisms of biological functions.

MATERIALS AND METHODS

Structural data

We considered three groups of toroidal proteins, namely, the DNA sliding clamps, NCPs, and TRAPs (Fig. 1). As structural data for the respective dimeric and trimeric β-clamps, we used the structures resolved for *E. coli* (β-clamps complexed with dsDNA, Protein Data Bank, PDB: 3BEP (7); and apo, PDB: 1MMI (52)) and human PCNAs (complexed with dsDNA, PDB: 6GIS (9); and apo, PDB: 1AXC (8)). We also used the β-clamp from *E. coli* resolved with a long dsDNA on the polymerase III side (PDB: 5FKV) (53) for further studies. To this aim, we modeled the long dsDNA on the other side of the clamp by extending the structurally resolved fragment to span both sides of the β-clamp. Furthermore, the closed (PDB: 3U61) (54) and open (PDB: 3U60) (54) structures of the trimeric clamp from T4 bacteriophage, which are both complexed with dsDNA and the clamp loader (ATP-driven multiprotein machines that couple ATP hydrolysis to the opening and closing of clamp around dsDNA), were used to evaluate the mechanism of action of the clamp loader. NCP structures used in our analysis were those from RVF virus in tetrameric (PDB: 4H5P) (11), pentameric (PDB: 4H5O) (11), and hexameric (PDB: 4V9E) (11) states complexed with RNA. Finally, for input structures, we used the TRAP undecamer from *Geobacillus stearothermophilus* as the naturally occurring oligomer (complexed with RNA, PDB: 1C9S) (55) as well as TRAP engineered to form a dodecamer (apo, PDB: 2EXT) (14).

Fig. S1 presents a quantitative analysis of the structural similarities between the members in different oligomerization states within each of these three families. Fig. S1 *a* illustrates the superposition of the dimeric and trimeric β-clamps, which exhibit a very close structural alignment except for the loops or disordered fragments between the repeat units. A large root mean-square deviation (RMSD) (3.8 Å) is calculated between the two structures because of these segments. Maps in Fig. S1, *b* and *c*, on the other hand, display the RMSDs between all pairs of subunits for the respective families NCP 4–6 and TRAP 11 and 12. Blocks along the diagonal refer to subunit pairs within the same oligomer, whereas off-diagonal blocks refer to those belonging to different oligomers. The pairwise RMSDs remain smaller than 1.0 Å in both cases.

ANM and GNM evaluation of collective dynamics

Here, we provide a brief summary on the anisotropic network model (ANM) (36) and Gaussian network model (GNM) (37) (see earlier work (56,57) for details). In both ENMs, each amino acid is represented by a node placed at its C_α coordinate (58,59). For modeling DNA/RNA molecules, each nucleotide is represented by three nodes: P (phosphate group), C4′ (base group), and C2 (sugar group) (58,59). Node pairs within a cutoff distance (r_c) of 15 Å (ANM) or 10 Å (GNM) are connected by springs of uniform force constant γ. Previous comparisons showed satisfactory agreement between theoretical and experimental B-factors using these respective cutoffs (32,36,58). A cutoff distance of 10 Å connects all neighboring residues within the first coordination shell in crystal structures (60). The higher cutoff distance in ANM provides better correlations for this three-dimensional (3D) model with anisotropic fluctuations in the x, y, and z directions.

In the GNM, residue fluctuations are isotropic by definition. Thus, the GNM provides information on the relative sizes of residue fluctuations and their cross correlations, but not their directions in 3D space. The system is represented by an $N \times N$ Kirchhoff/connectivity matrix, the eigenvalue decomposition of which yields $(N-1)$ nonzero modes of motion (37), each characterized by a mode shape (eigenvector, N-dimensional vector of the displacements of the N nodes along the mode coordinate) and a frequency (eigenvalue). 3D motions are predicted by the ANM, which is based on the decomposition of the $3N \times 3N$ Hessian, using normal mode analysis. In that case, for a network of N nodes, a $3N \times 3N$ Hessian matrix $\mathbf{H}$ is analytically calculated based on the crystal structure. Diagonalization of $\mathbf{H}$ yields $(3N-6)$ nonzero eigenvalues (λ_k) and the corresponding eigenvectors, $\boldsymbol{u}_k$. λ_k and $\boldsymbol{u}_k$ describe the frequency and shape (normalized distribution of node displacements) along the k^{th} normal mode, respectively. The modes are indexed in ascending order ($1 \le k \le 3N-6$) with increasing frequency. The first nonzero eigenvalue, λ_1, and corresponding eigenvector, $\boldsymbol{u}_1$, describe the lowest-frequency mode. The modes with the lowest frequencies are called the softest modes and define the most cooperative or global motions uniquely defined by the overall architecture. Here, we focused on the first 20 modes as a reasonable set representing the most collective conformational changes that are often implicated in the functional dynamics of proteins (27,34). In general, we use the GNM for predicting mean-square fluctuations (MSFs) and cross correlations because the GNM is highly robust and efficient (58); we use the ANM for predicting the mechanisms of motions (e.g., generating videos), which cannot be deduced from the GNM. All GNM and ANM analyses were performed using the ProDy package (61) and the DynOmics server (59).

Effect of DNA/RNA or substrate binding, or multimerization, on dynamics

The *env*ANM module of ProDy is used to evaluate the dynamics of a system (s) in the presence of an environment (e). Here, s is the toroidal protein (e.g., β-clamp), and e is the binding DNA/RNA or binding protein (e.g., clamp loader). Also, for investigating the effect of oligomerization on the intrinsic dynamics of a given subunit s, we use again the *env*ANM module, this time assuming all "other" subunits to represent the environment e. The pseudo-Hessian ($\overline{\mathbf{H}} = \mathbf{H}_{ss} - \mathbf{H}_{se}\mathbf{H}_{ee}{}^{-1}\mathbf{H}_{se}{}^{\mathrm{T}}$) describes the dynamics of the system s in the presence of the environment (57,59,62,63). Here, $\mathbf{H}_{ss}$, $\mathbf{H}_{se}$ and $\mathbf{H}_{ee}$ refer to s-s, s-e, and e-e submatrices of the Hessian $\mathbf{H}$ as follows:

$$\mathbf{H} = \begin{bmatrix} \mathbf{H}_{ss} & \mathbf{H}_{se} \\ \mathbf{H}_{se} & \mathbf{H}_{ee} \end{bmatrix} \tag{1}$$

Similarly, the pseudo-Kirchhoff matrix $\overline{\boldsymbol{\Gamma}} = [\boldsymbol{\Gamma}_{ss} - \boldsymbol{\Gamma}_{se}\boldsymbol{\Gamma}_{ee}^{-1}\boldsymbol{\Gamma}_{se}^{\mathrm{T}}]$ is used in *env*GNM (59).

Pairwise correlation cosines between modes accessible in different states

The extent of similarity, or overlap, between modes $\boldsymbol{u}_i$ and $\boldsymbol{v}_j$is measured by the pairwise correlation cosine or scalar product $\boldsymbol{u}_i \cdot \boldsymbol{v}_j$. Here $\boldsymbol{u}_i$ designates the i^{th} eigenvector of system/state A, and $\boldsymbol{v}_j$ designates the j^{th} eigenvector of B. Systems A and B can be, for example, the toroidal protein in the absence and presence of DNA. Given that the eigenvectors are normalized, the correlation cosine $\boldsymbol{u}_i \cdot \boldsymbol{v}_j$ varies in the range $[-1, 1]$, the two limits corresponding to fully anticorrelated (same direction, opposite sense) and fully correlated (same direction, same sense) motions; and $\boldsymbol{u}_i \cdot \boldsymbol{v}_j = 0$ for uncorrelated movements. The overlap between two GNM modes is the correlation cosine between the N-dimensional eigenvectors associated with these modes. Pairwise correlations are conveniently described by overlap matrices in the form of heat maps, in which the two axes correspond to the mode indices.

Overlap between mode spectra of A and B for selected frequency windows

The overlap between the first k modes accessible to states A and B is quantified as follows:

$$Overlap(k) = \left(\frac{1}{k} \sum_{i=1}^{k} \sum_{j=1}^{k} (\boldsymbol{u}_i \cdot \boldsymbol{v}_j)^2 \right)^{1/2}, \quad (2)$$

where the summations are performed over the subspace of selected modes.

Cumulative overlaps between experimental and theoretical data

Consider the structural change ($\Delta \boldsymbol{r}$: deformation vector) between the initial and final states of the protein, such as the difference between the experimentally determined bound and unbound forms, after optimal superposition of the two structures. The agreement between $\Delta \boldsymbol{r}$ and the i^{th} ANM mode accessible to the initial state is quantified by the correlation cosine (33) as follows:

$$S_i(exp) = |\Delta \boldsymbol{r} \cdot \boldsymbol{u}_i| / |\Delta \boldsymbol{r}|. \quad (3)$$

S_i(exp) varies in the range [0, 1] and provides a measure of the contribution of mode i to the experimentally observed change. The cumulative overlap measures how well a subset of low-frequency ANM modes (e.g., k of them) predicts the change $\Delta \boldsymbol{r}$ as (39):

$$CS(k) = \left(\sum_{i=1}^{k} [Si\ (exp)]^2 \right)^{1/2} = \left(\sum_{i=1}^{k} \left(\frac{\Delta \boldsymbol{r} \cdot \boldsymbol{u}_i}{|\Delta \boldsymbol{r}|} \right)^2 \right)^{1/2}, \quad (4)$$

where $CS(m) = 1$ for $m = 3N-6$ for a network of N nodes.

Mechanical stiffness analysis

Mechanical stiffness is computed following the MechStiff protocol described previously (36,64). The mean stiffness for residue i is calculated as the average over its effective force constant in response to uniaxial deformation exerted along (i, j) residue pairs, averaged over all pairs ($1 \leq j \leq N$). MechStiff analysis permits us to estimate the mechanical strength of the subunits and interfaces in different oligomerization states. The calculations were performed using the MechStiff module in ProDy (61).

Data visualization

The figures and videos were prepared using the DynOmics server (59) and PyMol package (65). In DynOmics, the structures are successively deformed along ANM modes to generate the videos, and the energy of each frame was minimized using CHARMM 36 force field for 700 steps (66). Plots were prepared using the Python matplotlib library (67).

RESULTS AND DISCUSSION

Toroidal architecture intrinsically favors cooperative saddle-like bending, rolling, counter rolling, stretching/contraction, breathing, and clamshell-like motions of the torus

We first examined the global modes of motion intrinsically accessible to toroidal proteins. Global modes refer to the lowest-frequency, usually most cooperative, modes uniquely defined by each architecture in the absence of ligands. Previous studies (16,18,19) have identified certain global motions for TRAP and the sliding clamps. Here, we present a more complete comparative analysis of the 16 lowest-frequency modes accessible to each of the toroidal structures in both unbound and bound (to DNA/RNA) forms to identify shared mechanisms as well as those unique to their specific DNA/RNA-binding, subunit packings, or oligomerization states. Table 1 presents a summary of global modes observed for the investigated eight structures, which are described in detail below and displayed in Video S1.

Among the toroidal multimers examined here, TRAPs are the most perfect toroidal systems, and their global dynamics is presented in Fig. 2 and Video S1 as a model/reference for movements intrinsically favored by the toroidal architecture. These global motions, mainly saddle-like bending, rolling, counter rolling, in-plane stretching/contraction, clamshell-like opening/closure, and breathing motions, also recur with minor alterations in many toroidal structures (see Table 1).

A closer look at the first (doubly degenerate) mode ($k = 1$ and 2; Fig. 2 *a*) shows that this mode induces out-of-plane opposite direction displacements along two perpendicular directions, resulting in a saddle-like bending in the originally planar torus (see also Video S1). All three families exhibit this type of motion, as shown in Fig. S2 and Video S2 for representative members. Regions colored red undergo bending movements, whereas those colored blue are practically rigid, and the arrows indicate the direction of motions. Different families adapt to this global movement in slightly modified forms; for example, in TRAP-12 and clamp dimer, the fluctuations are symmetrically deployed along both directions of the z axis such that the movement viewed from the top and bottom are almost identical, whereas in NCP-4, it is mainly confined to the top surface, with the lower surface serving as a scaffold. Yet the periodicity of the motion, or the basic four-repeat pattern of red and blue regions along the toroid, with alternating (up and down) out-of-plane fluctuations, is shared.

The second class of motion, commonly observed in modes $k = 3$ and 4, is an in-plane deformation (stretching and contraction along perpendicular directions) of the ring, which distorts the shape from circular to elliptical (see Fig. 2 *d*; Video S1). Pairs of modes describing stretching/contraction are shown in Fig. S3 for representative members from the other two families of proteins, mainly dimeric clamp and pentameric NCP. These modes would be twofold degenerate and lead to cylindrical symmetry if the PDB coordinates were fully symmetric. Like out-of-plane bending, this motion also contains four stationary wave nodes (WNs) (19) that consist of a collection of relatively immobile residues (Fig. S3 *a*, see the regions colored *blue*) separating those (*red*) moving outward or inward in the toroidal plane.

We also observe the rolling and breathing modes that have appeared in previous ENM studies on toroidal

TABLE 1 Classification of Global Motions and Corresponding Mode Numbers for Toroidal Proteins in the Unliganded (Apo) and Complexed (with RNA/DNA) Forms

Classification[a]	TRAP-11	TRAP-12	Clamp-2 (β-clamp)	Clamp-3 (PCNA)	NCP-6	NCP-4	NCP-5
PDB ID	1C9S[b]	2EXT[c]	1MMI	1AXC	4V9E[d]	4H5P[d]	4H5O[d]
	1C9S		3BEP	6GIS	4V9E	4H5P	4H5O
Saddle-like bending, 4 WNs[f]	1, 2	1, 2	1, 2	1, 2	1, 2	1, 13	1[e], 2[e]
	1, 2		1, 2	1, 2	1, 2	1, 16	1[e], 2[e]
Stretching-contraction,4 WNs	3, 4	3, 4	3, 4	3, 4	5[g], 6[g]	5	4[e], 5[e]
	3, 4		4, 6	4, 5	3[g], 4[g]	3, 11[g]	3[e], 4[e]
Rolling	5	5	5	5	4	6	-
	5		3[h]	3[h]	5	6	5
Saddle-like bending, 6 WNs	6, 7	6, 7	6	6	3	-	-
	6, 7		5	6	6	-	-
Counter-rolling	8, 9	8, 9	7, 8	7, 8	7, 8	8, 9	-
	8, 9		7[h], 8[h]	7[h], 12[h]	7, 8	12,13	-
Breathing	10	10	11[f]	13[i]	15[i]	15[i]	-
	10		16[f]	-	12[i]	14	15[i]
Stretching-contraction,6 WNs	11, 12	11, 12	9[g], 10[g]	9[g], 10[g]	14[g]	-	-
	15, 16		-	-	14[g]	-	-
Clamshell	13, 14	13, 14	14, 16	11, 12	10, 11	-	-
	11, 12		9/13, 14[h]	10, 11	10, 11	-	-
Saddle-like bending, 8 WNs	15, 16	15, 16	-	-	-	-	-
	13, 14		-	-	-	-	-

[a]The second row/line of mode numbers refer to the complex in each case.
[b]Apo and complex structures are from two biological assemblies #1 and #2 of the same PDB, respectively.
[c]Only the apo structure is available for TRAP-12.
[d]Apo structure is extracted from the complex by removing the RNA or DNA segment.
[e]One of the five subunits is either stationary or two of the neighboring subunits move together in modes with four nodes (Fig. S2).
[f]WNs (wave nodes) correspond to clusters of residues that are relatively immobile.
[g]This mode includes rotational motion, which differentiates it from its counterpart—the perfect in-plane motion—observed in TRAPs.
[h]This mode becomes asymmetric in the complex with DNA (Fig. 3).
[i]This is not a fully concerted breathing mode, because of some stationary nodes and/or slight out-of-plane aspect due to rotational motion of the subunits (Fig. S3).

proteins as nondegenerate modes invariant under rotations about the central axis (16,18,19,25). The rolling motion (Fig. 2 *b* and Video S1) mostly observed in the fifth mode (Table 1) corresponds to whirling motions around the circumference of the torus. The uniform breathing motion observed in the 10th or higher modes causes an expansion/contraction of the ring including its central pore (Figs. 2 *f* and S4; Video S1). Finally, out-of-plane and in-plane motions with higher number of WNs (6 or 8) also exist among the first 16 modes. Such motions also appear in pairs consistent with the rotations around the central axis (25).

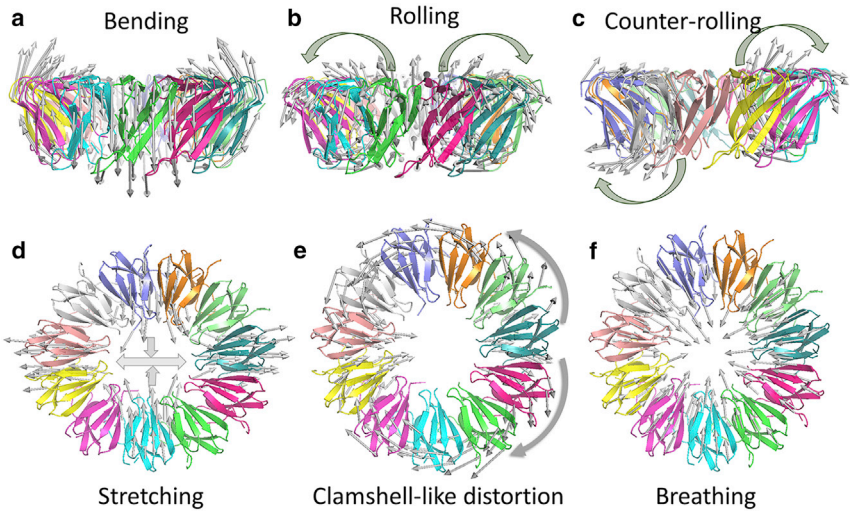

FIGURE 2 Global modes of motions typically favored by toroidal architecture illustrated for TRAP-11 (PDB: 1C9S). (*a*) The out-of-plane, bending motion in modes 1 and 2, (*b*) the nondegenerate, rolling motion in mode 5, (*c*) the counter-rolling motions in modes 8 and 9, (*d*) the in-plane, stretching/contraction motions in modes 3 and 4, (*e*) the in-plane, clamshell-like motions in modes 13 and 14, and (*f*) the nondegenerate, radial breathing motion in mode 10 are shown. The thick arrows indicate the displacements of residues along the ANM modes, whereas gray arrows are added to clarify the global deformation directions. See Video S1 for the animations of these modes. To see this figure in color, go online.

Global modes listed for TRAPs are in conformity with the modes of a perfectly uniform torus formed by equally spaced nodes, as observed in the analysis of the nuclear pore complex at a coarse-grained scale (25). Yet, to our knowledge, some new motions are identified in this work such as counter rolling (Fig. 2 *c*) and clamshell-like opening/closure (Fig. 2 *e*), which may allow for the "opening/unraveling" of the multimer (see Video S1). The functional implications of these modes will be described in the context of the machinery of sliding clamps.

As the oligomeric topology diverts from almost perfect symmetry observed in TRAPs to a certain degree of asymmetry in clamps and more markedly in NCPs, the categorization of modes becomes less clear. Some global motions are either modified or not observed among the first 16 modes of NCP tetramers and pentamers (Figs. S2 *c*, S3 *c*, and S4 *b*; Table 1). Still among the NCPs, the hexamer displays most of the typical toroidal motions because of its tighter interfaces and relatively more uniform mass distribution. The effect of nonuniform mass distribution on toroidal motions has been discussed in our previous work on nuclear pore complex (25).

Intrinsically shared modes of toroidal proteins are selectively recruited, altered, or suppressed upon complexation with DNA or RNA

Toroidal proteins form different types of complexes with DNA or RNA (Fig. 1). The sliding clamp dimer and the trimeric clamp PCNA encircle the dsDNA (Fig. 1, *a* and *b*), whereas an ssRNA binds along the inner face of the NCPs (Fig. 1, *c–e*) or wraps around the TRAP as a continuous ring (Fig. 1 *f*). Herein, we investigate how the dynamics of these proteins are altered upon binding DNA/RNA. Table 1 provides a summary of the operating modes in the apo and complexed forms, showing that complexation may have three different types of effects: 1) changing the prior probabilities or frequencies of available collective modes with minor alterations in mode mechanisms, 2) obstructing/blocking certain modes, and 3) retaining some modes unchanged. Notably, those changes favor/facilitate functional mechanisms as described below.

The heat map in Fig. 3 *a* illustrates the extent of overlap between the global modes accessible to *E. coli* β-clamp dimer before and after formation of a complex with dsDNA. The abscissa and ordinate refer to the respective mode numbers $k = 1–15$ accessible to the clamp dimer in dsDNA-unbound and -bound forms, respectively, and the entries represent the absolute values of the pairwise correlation cosines between these two sets (see Materials and Methods). In the extreme case of no effect on the global modes, one would expect dark red entries (fully correlated modes) along the diagonal and dark blue (uncorrelated modes) elsewhere. Instead, we observe an increasingly diffuse distribution of partially correlated modes, with correlations weakening with increasing mode numbers. Except for the first two modes, which remain practically unchanged

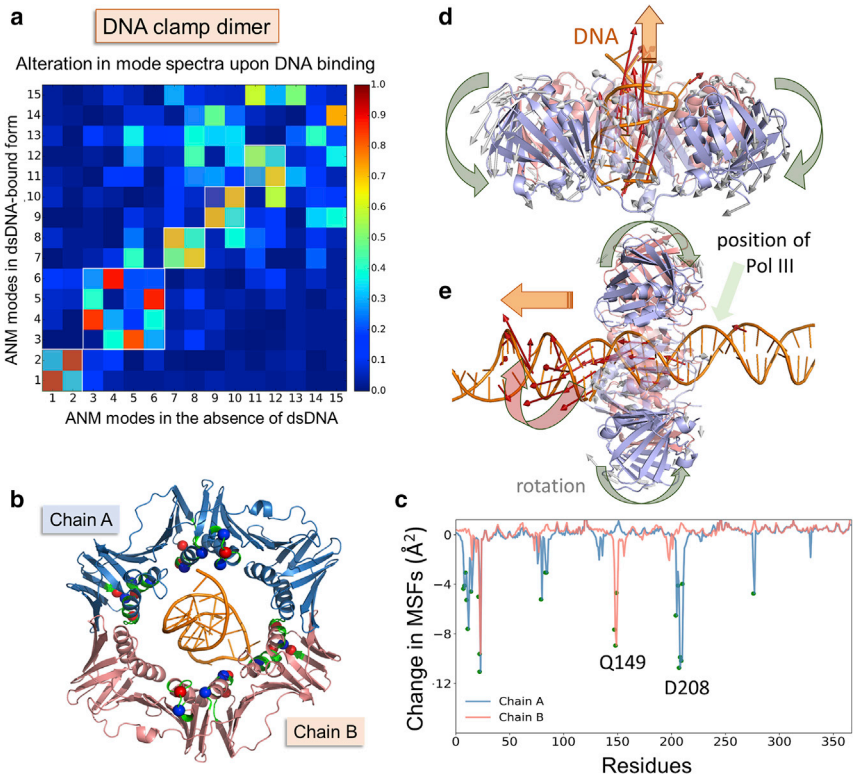

FIGURE 3 Modification of β-clamp dynamics upon binding dsDNA. (*a*) The level of overlap between the global modes of motion intrinsically accessible to β-clamp in unbound form and its global modes in the complex with dsDNA are shown. The entries in the heat map display the correlation cosines between the top-ranking 15 modes in each case (see the *bar* on the *right*). (*b* and *c*) Change in MSFs of clamp residues induced upon binding to dsDNA are shown. The change in MSFs in (*c*) are evaluated by taking the difference between GNM and *env*GNM (with dsDNA as environment) results. The curves in blue and pink display the results for subunits A and B, respectively, also shown by the same colors in (*b*). Negative values (*ordinate*) refer to suppression in mobility due to bound dsDNA. The residues showing notable suppressions (ΔMSF > 3.0 Å^2) are indicated by green dots on the graph and on the structure of the complex (*b*). Among them, the positively and negatively charged residues are shown in blue and red spheres, respectively. dsDNA is colored orange. (*d* and *e*) The processivity activities of the sliding clamp are accomplished through the global rolling (mode 5) already accessible in the absence of dsDNA, which is promoted in the complex with the short (*d*) and long (*e*) dsDNA to respective modes 3 and 19 (see *a* and Fig. S6). See also corresponding Videos S3 and S4. To see this figure in color, go online.

(the third effect mentioned in the above paragraph), the collective modes are clearly altered (first effect) or suppressed (second effect) upon complexation. Of interest is the first effect, manifested by mode swapping and/or rearrangements/perturbations. White boxes along the diagonal indicate such cases. For example, the breathing motion (originally mode $k = 11$) moves to higher (relatively less prominent or stiffer) mode $k = 16$ (see also Table 1) because the large central hole of the torus (diameter = 35 Å) is mostly occupied by the dsDNA molecule (diameter = 24 Å).

We examined the change in the fluctuation profile of DNA β-clamp residues induced upon binding the dsDNA. The dsDNA tilts with an angle ($\sim$22°) as it passes through the ring structure of the clamp (7). As a result, the mobilities of the two subunits, colored pink and blue in Fig. 3 *b*, are differentially affected. As shown Fig. 3 *c*, the decreases in the MSFs of residues resulting from dsDNA binding are different between subunits A and B. The mobilities of certain residues (e.g., Q149 in subunit A and D208 in subunit B) are severely decreased, which is because of their position near the dsDNA binding interface (Fig. 3 *b*). Mutations at the positions 148–152 have been reported to impair the DNA loading by impairing the clamp-DNA interaction (68).

The trimeric clamp PCNA dynamics also showed a dependency on DNA binding similar to that of β-clamp, and the three subunits exhibited different levels of changes in their MSF profiles (Fig. S5, *a* and *b*). In contrast to DNA clamps, TRAP-11 global modes were found to be relatively robust (i.e., minimally affected by RNA binding) as illustrated in Fig. S5, *g* and *h*. NCPs showed a diverse behavior. Whereas NCP-4 dynamics was substantially modified by RNA binding (Fig. S5, *c* and *d*), the global motions of NCP-6 were minimally affected (Fig. S5, *e*–*h*). In fact, RNA binding stabilizes the internal toroidal surface and interactions, thereby recovering the slowest six modes of motion typical of the toroidal shape (Table 1). In other words, RNA binding to NCP-6 consolidates the global motions that are intrinsically accessible to toroidal proteins as typified by TRAPs.

DNA binding enhances the rolling mode accessible in the unbound β-clamp, thus promoting or self-regulating DNA processivity

The rolling mode is unique as a highly collective and easily accessible (soft) mode that engages the entire toroid. This nondegenerate mode rotates the nodes around the toroid's surface such that the inner nodes move "up" along the z direction, that is, perpendicular to the torus plane (Fig. 3 *d* and Video S3), and the outer nodes move "down." In the complex with dsDNA, this motion may become more prevalent as it shifts to the third mode from the fifth mode without the DNA in both clamps. A decrease in mode number generally means an increased ability to deploy such a structural change, with modes with smaller indices being "softer" or energetically more favorable. Thus, dsDNA binding assists the clamp in undergoing its function, the dsDNA serving as a self-regulator of its processivity. Fig. 3 *d* illustrates how this mode promotes the mechanical sliding of the toroidal structure relative to the threading of dsDNA through the hole. Changes in residue-residue contacts between the DNA and the β-clamp structures occurring during the rolling motion are shown in Video S4. Some contacts are formed, whereas others are broken, during the translocation of dsDNA through the hole. Five residues, Gly19, Gly23, Arg24, Arg205, and Gly210, appear to form stable interactions with the sliding long dsDNA.

Notably, the sliding/translocation movement of the β-clamp relative to the dsDNA is accompanied by the rotation of the dsDNA, which can be clearly seen in the cross-sectional view of the motion in the presence of a long dsDNA segment (Video S4). Indeed, in the presence of a long DNA segment, the rolling motion shifts to mode 19 because the slowest modes are dominated by swinging motions of the long dsDNA tails (Fig. S6). The coupling of clamp rolling (ANM mode 19) to the rotation of long dsDNA is in line with the cogwheel sliding mechanism of the clamp, previously identified by structure determination and single molecule measurements (9,69,70). This motion has been also named as helical sliding or rotation-coupled sliding of the clamp along DNA.

β-clamp clamshell-like motions that facilitate dsDNA processivity are allosterically enhanced by the clamp loader

Opening of the sliding clamp to load onto dsDNA is facilitated by its complex formation with the clamp loader (Fig. 4, *a* and *b*). A mismatch in the complex formed between the pentameric clamp loader and the six repeats of the sliding clamp has been pointed out to promote clamp opening (54,71). Our ANM analysis points to selected modes that aid in this process. At this point, we divert to the available structures of the closed (PDB: 3U60) and open (PDB: 3U61) clamp from T4 bacteriophage, which have been solved in complex with the clamp loader and the primer-template DNA (54). This clamp consists of three subunits because it is the human counterpart of PCNA; it has a triangular-like shape rather than a circular shape (Fig. 4). Earlier studies have considered that in-plane and out-of-plane motions of the toroid might enable clamp opening (72,73). However, we can now identify the specific ENM modes that assist in undergoing the functional changes in structure using the method described in Materials and Methods for the correlation between the experimentally detected change, $\Delta \boldsymbol{r}$, and the individual modes ($\boldsymbol{u}_i$) accessible to the original conformer (see Eqs. 3 and 4).

Structural alignment of the open (o) and closed (c) clamp structures resolved experimentally displays an RMSD of

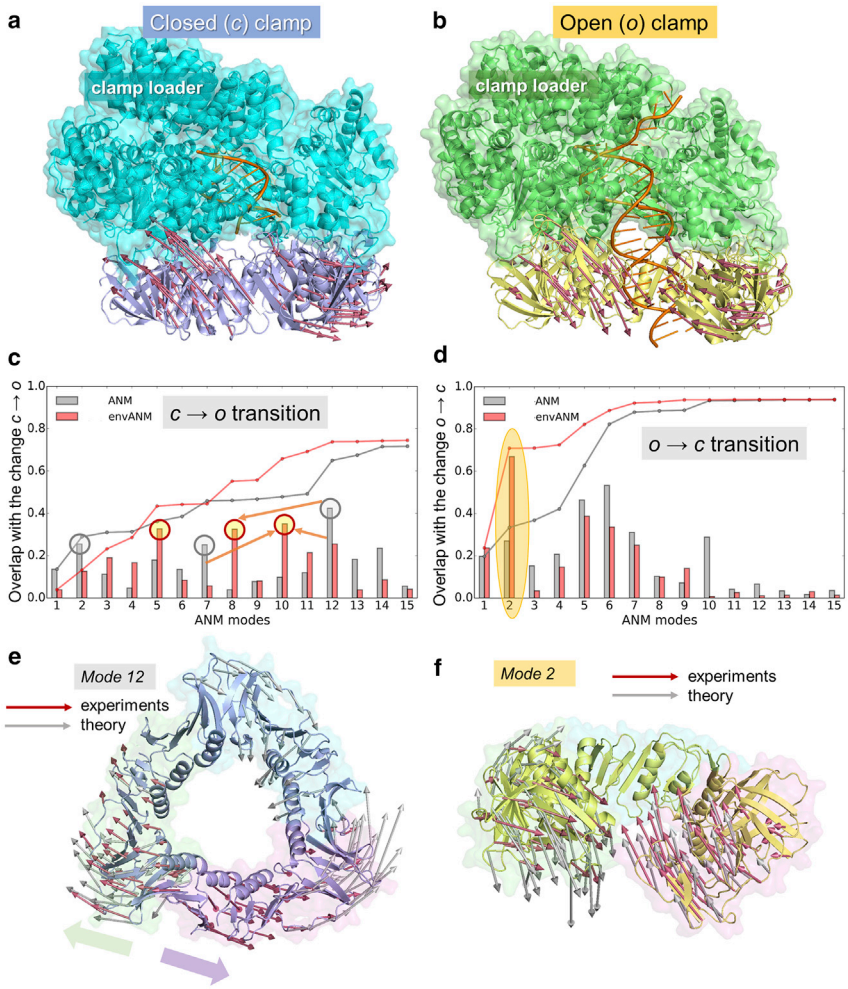

FIGURE 4 Opening/closure motions of the T4 bacteriophage clamp are enhanced by clamp loader binding. (*a*) Closed (*steel blue*, PDB: 3U61) (54) and (*b*) open (*yellow*, PDB: 3U60) (54) structures of the clamp are shown in complex with the clamp loader (*cyan* and *green*, respectively) and the dsDNA (*orange*). The arrows indicate the movements of residues in the closed-to-open ($c \rightarrow o$) and open-to-closed ($o \rightarrow c$) transitions, respectively. (*c* and *d*) Overlaps between the structural change accompanying both transitions and the intrinsically accessible global modes are shown for the isolated clamp (*gray bars;* ANM results) and for the clamp in the presence of the loader and DNA (*red bars*; *env*ANM results). The corresponding cumulative overlap curves are also displayed on the same panels. In (*c*), the three modes with high overlaps obtained by ANM and *env*ANM are highlighted in gray and red circles, respectively. Orange arrows indicate mode shifting among them. The higher overlaps (and cumulative overlap curves) in the presence of loader (and DNA) support the role of the loader as a facilitator of the functional opening/closing motions. (*e*) Clamshell-like (mode 12) and (*f*) out-of-plane fluctuations of clamp open ends (mode 2) promote clamp opening and closure, respectively. The diagrams display the theoretically predicted residue motions in these modes (*gray* arrows) in comparison to the structural changes experimentally observed (*red arrows*). The ribbons in (*e*) (*steel blue*) and (*f*) (*yellow*) are colored by the same colors as in (*a*) and (*b*), and the subunits are shown in transparent green, cyan, and pink surfaces. To see this figure in color, go online.

6.7 Å between the two forms. Both axial and radial displacements in the subunits are observed between the two forms as indicated by the arrows in Fig. 4, *a* and *b*. To observe whether these functional changes in conformation are encoded in the intrinsic dynamics of the bacteriophage T4 clamp structure, we first considered the closed (*c*) clamp without the clamp loader and the DNA and evaluated the individual and cumulative overlaps between the modes intrinsically accessible based on the ANM and the structural change $\Delta \boldsymbol{r}(c \rightarrow o)$ involved in clamp opening. Fig. 4 *c* displays the correlation cosines (Eq. 3, *bars*) between the predicted soft modes and the experimentally observed $\Delta \boldsymbol{r}$ during the transition $c \rightarrow o$. The curves show the cumulative correlations (Eq. 4) summed up over 15 soft modes intrinsically accessible to the clamp in isolation (*gray curve*) and in the presence of the clamp loader and DNA (*red curve*). Results are shown for two opposite transitions, opening and closure ($c \rightarrow o$ and $o \rightarrow c$), in the respective Fig. 4, *c* and *d*.

Two important conclusions are drawn from Fig. 4, *c* and *d*. First, before interpreting these results, we recall that the complete set of $3N-6$ modes spans the full space of changes on the conformational landscape such that the cumulative overlap summed over all modes is 1. Here, we see that the first 15 modes are sufficient to reach a cumulative overlap of ~0.70 (Fig. 4 *c*); and in the case of clamp closure, the first 10 modes achieve a correlation of ~0.95. The 12th mode of *c*, indicated by the gray circle and illustrated in Fig. 4 *e*, is a clamshell-like motion facilitating the passage $c \rightarrow o$ in the absence of clamp loader and DNA. Fig. 4 *e* illustrates the good agreement between residue motions driven by this mode (*gray arrows*) and the experimentally observed changes (*red arrows*) during this transition. Two other modes of *c* calculated with ANM, namely, the second (saddle-like bending) and seventh mode (counter rolling, not shown), act as drivers of the vertical displacements during opening. These results provide evidence for the intrinsic ability of the clamp architecture to favor a concerted opening for binding and processing DNA by simply moving along its softest modes. In fact, the bacteriophage T4 clamp has been shown to fluctuate between open and closed states by itself in solution (74).

Second, when the clamp loader and DNA are included in the computational analysis as environment using *env*ANM, several modes that contribute to clamp opening/closure are altered to yield higher overlap with experimentally observed

changes as can be observed in Fig. 4, *c* and *d*. The clamshell-like mode (now shifted to the 8th mode) of *c* together with the 5th mode (combined rolling and breathing) and 10th mode (combined counter-rolling and clamshell-like motions) further facilitate the opening of the clamp in the presence of the loader (Fig. 4 *c*, see the *red circles*). Interestingly, the presence of the loader and DNA modifies the dynamics of the open clamp even more strongly (Fig. 4 *d*) to enhance clamp closure in remarkable agreement with experiments: a correlation cosine of 0.65 achieved by a single mode, the second mode, which induces out-of-plane opposite direction fluctuations at the two ends of the open clamp (Fig. 4 *f*) via a combined counter rolling and twisted opening/closing (see Fig. 2 *c*).

Further analysis of clamp dynamics in the presence of the clamp loader but in absence of dsDNA (Fig. S7) shows very similar effects to those observed in Fig. 4, *c* and *d* in the presence of dsDNA, further demonstrating that the observed enhancement of functional motions is actually driven by the clamp loader. Binding of the clamp loader thus allosterically stimulates the activation of the collective motions that enhance the processivity of dsDNA by the T4 bacteriophage clamp.

Modular dynamics of the subunits support the global motions of the toroids

Next, we analyzed the extent to which the intrinsic dynamics of an isolated subunit is altered upon oligomerization. Fig. S8 shows that the global modes are conserved to a large extent in the dimeric and trimeric clamps as well as NCP-6 (respective Fig. S8, *a–c*). TRAP-11, on the other hand, retains the top five modes but not higher modes (Fig. S8 *d*). The changes in MSFs upon oligomerization (Fig. S8, *e–h*) show the residues whose fluctuations are most strongly suppressed by interfacial interactions. β-clamp L82, neighboring to the minimum at G81 (Fig. S8 *e*) has been reported to affect both the dimerization state and thermostability of the β-clamp (23).

To quantify the impact of oligomerization, we used two metrics. First, we evaluated the ratio of interfacial residues to all residues to test whether the observed effects could be related to the relative population of interfacial residues (Table S1, *column 5*; see also Fig. 5 *f*). This clearly shows that the majority of TRAP residues (64% in TRAP-11 and 52% TRAP-12) takes part in interfacial interactions, hence the strong perturbation in the intrinsic dynamics of the subunit. This behavior is also confirmed by the second metric, the overlap between the soft GNM modes accessible to the isolated subunit and those accessible to the subunit in the oligomer. Column 6 in Table S1 shows the smallest overlaps in the case of TRAPs. However, all toroidal subunits exhibit overlaps of 0.92 $\pm$ 0.01 between their monomeric and oligomeric state dynamics, which means that the modular dynamics of the subunits is closely maintained in the oligomer.

Overall, the close preservation of the intrinsic dynamics of isolated subunits in the oligomers points to the functional

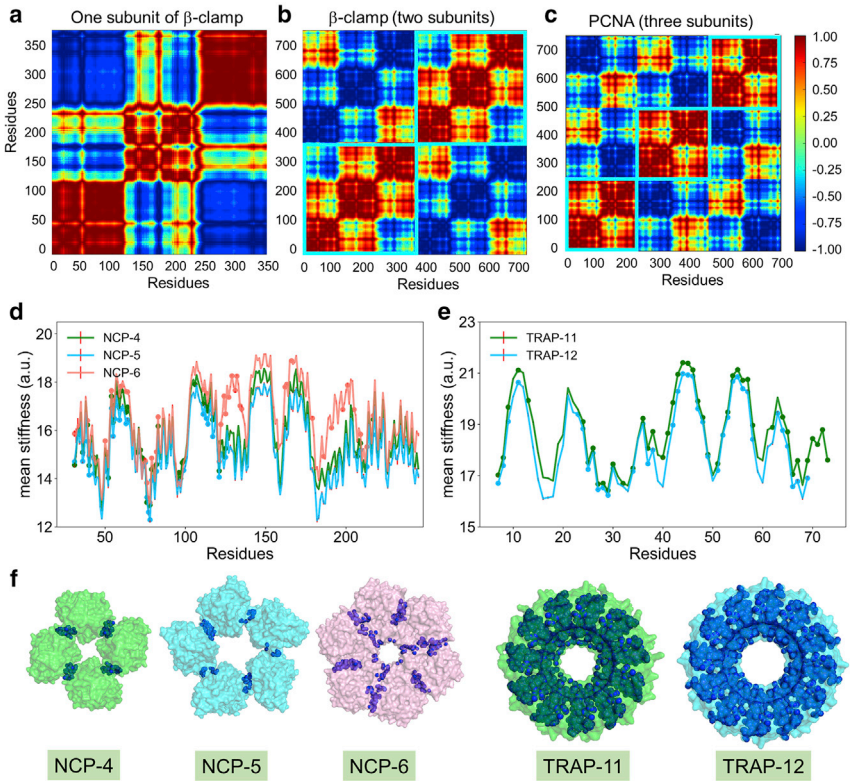

FIGURE 5 Effect of oligomerization on the intrinsic dynamics and mechanics of toroidal proteins. (*a–c*) Cross correlations driven by the softest two modes between all residue pairs in (*a*) an isolated DNA-clamp subunit, (*b*) two subunits in the DNA clamp, and (*c*) three subunits in PCNA are shown. In (*b*) and (*c*) the intrasubunit correlations are enclosed in cyan squares. (*d* and *e*) Stiffnesses of (*d*) NCP and (*e*) TRAP residues in different oligomerization states are shown. The interfacial residues are labeled with dots. These residues are those making intersubunit contacts within a cutoff distance of 4 Å between heavy atoms (except for the NCP N-terminal long helices that are integrated into the adjacent subunits). Minimal differences are observed between the different subunits in a given toroidal structure, indicated by red error bars that are hardly visible. (*f*) The regions making intersubunit contacts (*blue spheres*) are shown. The structures are represented as transparent surfaces colored by the corresponding curves in (*d*) and (*e*). NCP-6 and TRAP-11 have higher stiffnesses than the other members of their families, consistent with their higher natural abundance. See also Table S1. To see this figure in color, go online.

significance of their modular character. Oligomerization enables the cooperative deployment of the global motions that are encoded in the subunit fold; or, the intrinsic dynamics of the subunits support the global motions of the toroids.

The maps in Fig. 5 compare the inter-residue cross correlations for (Fig. 5 *a*) an isolated subunit of the β-clamp, (Fig. 5 *b*) two subunits in the β-clamp, and (Fig. 5 *c*) the three subunits in the PCNA. The diagonal cyan square outlines indicate the sequence ranges of the individual subunits in Fig. 5, *b* and *c*. The most concrete effect of dimerization into a toroidal structure is an increase in the positive correlations within subunits (evidenced by the fraction of *red* regions in Fig. 5 *a* compared to those in the *diagonal boxes* in Fig. 5, *b* and *c*). Fig. S9 displays the cross-correlation maps for NCPs. Notably, each subunit is highly coherent in NCP-4, -5, and -6, as apparent from the dark red blocks along the diagonal. This again indicates that each subunit retains its intrinsic character apart from the N-terminal helices that reach out to the adjacent subunit.

Finally, we analyzed the mechanical properties of the oligomers using MechStiff (64). The mean stiffness profiles of the three NCPs, each composed of the same subunits, share similar characteristics, but NCP-6 exhibits the highest resistance to mechanical stress (Fig. 5 *d*). Notably, the 6-mer NCP has been reported to be the most abundant NCP oligomer (10), consistent with the resistance to destabilization computed here. Similarly, TRAP-11 exhibits higher stiffness than TRAP-12 (Fig. 5 *e*). In accord with this result, only the wild-type 11-mer TRAP is highly stable and could be crystallized (14). The 12-mer TRAP has been engineered; it is not naturally observed (14).

Thus, in both NCP and TRAP oligomers, the computed relative stiffnesses of the different oligomeric states, which provide a measure of the relative stabilities of the structures, are consistent with the natural abundances/occurrences of selected oligomers.

CONCLUSIONS

This study presents a comparative analysis of the structural dynamics of toroidal proteins belonging to different families and stabilized in different oligomerization states (Fig. 1), with a focus on the role of global dynamics in enabling the mechanisms of function of DNA clamps. Major findings are presented below, along with a description of their broader significance.

Shared global dynamics

Toroidal proteins have access to well-defined mechanisms of global motions endowed by their unique architecture, exemplified by the global modes of motion of TRAP-11, illustrated in Fig. 2 and Video S1, and summarized in Table 1. Typical global motions include out-of-plane saddle-like bending, in-plane stretching, rolling and counter rolling, breathing, and clamshell-like opening/closing. These intrinsically accessible motions are shared by three families of toroidal proteins, DNA clamps, nucleocapsids, and TRAPs. Whereas DNA clamps and NCP-6 closely obey the general classification of global modes, members such as NCP-4 and NCP-5 exhibit variations, as illustrated in Figs. S2 and S4 and Video S2. We note that such variations in structural dynamics play an important role in the functional differentiation of the protein from a "promiscuous generalist into a specialist" (75). This is also consistent with a recent study demonstrating that an interplay between shared dynamics (usually the first four to five modes, as is also the case here; see Table 1) intrinsically defined by the fold and member-specific low-to-intermediate frequency modes determines the functional dynamics of family members (26).

The functionality of toroidal global modes is enhanced upon DNA or substrate protein binding, shown for DNA clamps in the presence of DNA duplex and/or clamp loader

It is broadly established that global dynamics favor functional motions involved in substrate binding or allosteric regulation (27,35,39,76). Yet proteins do not function in isolation. An extremely interesting observation made here upon focusing on DNA clamps is the role of bound DNA (Fig. 3) or clamp loader (Fig. 4) in enhancing the intrinsically accessible global motions to facilitate the functional mechanisms of the clamps.

In the former case (DNA binding), the rolling motions, which enable the sliding of the clamp against DNA in both β-clamp and PCNA, are rendered easier (softer) upon short DNA binding (see Fig. 3 *e* and Video S3). Threading of DNA through the clamp hole is mainly facilitated, if not driven, by the rolling mode of the β-clamp, which simultaneously induces a rotation of the dsDNA, as may be seen by the cross-sectional view in Video S4 for the clamp/long dsDNA complex. This motion is consistent with single-molecule diffusion data and structural analysis that showed that clamp proteins predominantly undergo rotation-coupled sliding along the DNA duplex (9,69,70).

In the latter case (Fig. 4), the clamp loader facilitates/favors the opening of the clamp to bind DNA. This event is predominantly controlled by the clamshell-like mode (Fig. 4, *c* and *e*). These results lend support to the "bind-open-lock" model in which the loader binds a closed state and then triggers conformational changes that drive the transition to and stabilization of the open form (77). Our study suggests that in addition to opening, the clamp loader plays a role in clamp closure too to stabilize the DNA-bound form. In that case, a saddle-like bending (mode 2) is found to be enhanced by the loader to facilitate clamp closure in the DNA duplex bound state (Fig. 4, *d* and *f*).

Overall, this study demonstrates that the DNA itself is involved in an allosteric autoregulation of its processivity by the β-clamp action upon promoting modes that enable β-clamp translocation; and in the case of PCNA, the clamp loader, in conformity with its biological role (54,71), allosterically and selectively enhances the modes that enable DNA duplex binding and unbinding.

Clamshell-like opening/closure of the torus emerges as an effective mode of motion that supports the change in the oligomerization state

It is interesting to note that clamshell-like motions that enable the opening/closure of the torus lie among soft (energetically accessible) collective modes. This type of opening is reminiscent of the mechanism observed for human CAMKII, which may transition between 12-meric and 14-meric states (two rings with 6 or 7 subunits each) through the addition or loss of a dimer (78). The predisposition of the structure to clamshell-like movement thus facilitates the opening of the ring to allow for the insertion of a new subunit or a DNA duplex.

Future prospects for protein design

Toroidal proteins have been selected as elements in designing supramolecular machines, such as artificial protein tubes (79) and cages (80) assembled from toroidal peroxiredoxin and TRAP, respectively. The revealed dynamics of toroidal proteins can be useful in designing such artificial machines. Our analysis demonstrates that structures with different mechanical and dynamic properties can be generated by using the same modular units but changing interfacial interactions or oligomerization states (Fig. 5). TRAPs present the tightest interfaces with the highest mechanical stiffness. As a result of their compact and almost perfect toroidal structures, the isolated subunit dynamics is modified to a large extent in the oligomeric TRAPs. This is in contrast to clamps and NCPs, which retain the modular dynamic characteristics of the individual subunits. The versatility of toroidal oligomers to adapt to different oligomerization states and select from a pool of cooperative motions with minor alterations may be further exploited in future designs of supramolecular machines.

SUPPORTING MATERIAL

Supporting Material can be found online at https://doi.org/10.1016/j.bpj.2020.01.046.

AUTHOR CONTRIBUTIONS

G.H. and I.B. designed the research. G.H. and H.L. performed the computations. G.H., H.L., and P.D. analyzed the corresponding results. G.H., H.L., P.D., and I.B. wrote the article.

ACKNOWLEDGMENTS

This work was supported by the National Natural Science Foundation of China (31872723 and 21336009), a project funded by the Priority Academic Program Development of Jiangsu Higher Education Institutions (PAPD), and the National Institutes of Health grants P30 DA035778 and P41 GM103712.

REFERENCES

1. Hingorani, M. M., and M. O'Donnell. 1998. Toroidal proteins: running rings around DNA. *Curr. Biol.* 8:R83–R86.
2. Hingorani, M. M., and M. O'Donnell. 2000. A tale of toroids in DNA metabolism. *Nat. Rev. Mol. Cell Biol.* 1:22–30.
3. Wilce, J., J. Vivian, and M. Wilce. 2012. Oligonucleotide binding proteins: the occurrence of dimer and multimer formation. *Adv. Exp. Med. Biol.* 747:91–104.
4. André, I., C. E. M. Strauss, …, D. Baker. 2008. Emergence of symmetry in homooligomeric biological assemblies. *Proc. Natl. Acad. Sci. USA.* 105:16148–16152.
5. Yan, W., G. Hu, and B. Shen. 2016. Network analysis of protein structures: the comparison of three topologies. *Curr. Bioinform.* 11:480–489.
6. Kong, X.-P., R. Onrust, …, J. Kuriyan. 1992. Three-dimensional structure of the β subunit of *E. coli* DNA polymerase III holoenzyme: a sliding DNA clamp. *Cell.* 69:425–437.
7. Georgescu, R. E., S.-S. Kim, …, M. O'Donnell. 2008. Structure of a sliding clamp on DNA. *Cell.* 132:43–54.
8. Gulbis, J. M., Z. Kelman, …, J. Kuriyan. 1996. Structure of the C-terminal region of p21(WAF1/CIP1) complexed with human PCNA. *Cell.* 87:297–306.
9. De March, M., N. Merino, …, A. De Biasio. 2017. Structural basis of human PCNA sliding on DNA. *Nat. Commun.* 8:13935.
10. Ferron, F., Z. Li, …, J. Lescar. 2011. The hexamer structure of Rift Valley fever virus nucleoprotein suggests a mechanism for its assembly into ribonucleoprotein complexes. *PLoS Pathog.* 7:e1002030.
11. Raymond, D. D., M. E. Piper, …, J. L. Smith. 2012. Phleboviruses encapsidate their genomes by sequestering RNA bases. *Proc. Natl. Acad. Sci. USA.* 109:19208–19213.
12. Raymond, D. D., M. E. Piper, …, J. L. Smith. 2010. Structure of the Rift Valley fever virus nucleocapsid protein reveals another architecture for RNA encapsidation. *Proc. Natl. Acad. Sci. USA.* 107:11769–11774.
13. Antson, A. A., J. Otridge, …, P. Gollnick. 1995. The structure of Trp RNA-binding attenuation protein. *Nature.* 374:693–700.
14. Heddle, J. G., T. Yokoyama, …, J. R. H. Tame. 2006. Rounding up: engineering 12-membered rings from the cyclic 11-mer TRAP. *Structure.* 14:925–933.
15. Oakley, A. J. 2016. Dynamics of open DNA sliding clamps. *PLoS One.* 11:e0154899.
16. Hu, G., S. Michielssens, …, A. Ceulemans. 2012. The harmonic analysis of cylindrically symmetric proteins: a comparison of Dronpa and a DNA sliding clamp. *J. Mol. Graph. Model.* 34:28–37.
17. Rydzewski, J., W. Strzalka, and W. Nowak. 2015. Nanomechanics of PCNA: a protein-made DNA sliding clamp. *Chem. Phys. Lett.* 634:236–242.
18. Hu, G., S. Michielssens, …, A. Ceulemans. 2011. Normal mode analysis of Trp RNA binding attenuation protein: structure and collective motions. *J. Chem. Inf. Model.* 51:2361–2371.
19. Matsunaga, Y., R. Koike, …, A. Kidera. 2012. Influence of structural symmetry on protein dynamics. *PLoS One.* 7:e50011.
20. Ivanov, I., B. R. Chapados, …, J. A. Tainer. 2006. Proliferating cell nuclear antigen loaded onto double-stranded DNA: dynamics, minor

groove interactions and functional implications. *Nucleic Acids Res.* 34:6023–6033.

21. Murtola, T., I. Vattulainen, and E. Falck. 2008. Insights into activation and RNA binding of Trp RNA-binding attenuation protein (TRAP) through all-atom simulations. *Proteins.* 71:1995–2011.
22. Purohit, A., J. K. England, …, M. Levitus. 2017. Electrostatic interactions at the dimer interface stabilize the E. coli β sliding clamp. *Biophys. J.* 113:794–804.
23. Koleva, B. N., H. Gokcan, …, P. J. Beuning. 2019. Dynamics of the E. coli β-clamp dimer interface and its influence on DNA loading. *Biophys. J.* 117:587–601.
24. Perumal, S. K., X. Xu, …, S. J. Benkovic. 2019. Recognition of a key anchor residue by a conserved hydrophobic pocket ensures subunit interface integrity in DNA clamps. *J. Mol. Biol.* 431:2493–2510.
25. Lezon, T. R., A. Sali, and I. Bahar. 2009. Global motions of the nuclear pore complex: insights from elastic network models. *PLoS Comput. Biol.* 5:e1000496.
26. Zhang, S., H. Li, …, I. Bahar. 2019. Shared signature dynamics tempered by local fluctuations enables fold adaptability and specificity. *Mol. Biol. Evol.* 36:2053–2068.
27. Tiwari, S. P., and N. Reuter. 2018. Conservation of intrinsic dynamics in proteins-what have computational models taught us? *Curr. Opin. Struct. Biol.* 50:75–81.
28. Nevin Gerek, Z., S. Kumar, and S. Banu Ozkan. 2013. Structural dynamics flexibility informs function and evolution at a proteome scale. *Evol. Appl.* 6:423–433.
29. Tirion, M. M. 1996. Large amplitude elastic motions in proteins from a single-parameter, atomic analysis. *Phys. Rev. Lett.* 77:1905–1908.
30. Bahar, I., A. R. Atilgan, and B. Erman. 1997. Direct evaluation of thermal fluctuations in proteins using a single-parameter harmonic potential. *Fold. Des.* 2:173–181.
31. Hinsen, K. 1998. Analysis of domain motions by approximate normal mode calculations. *Proteins.* 33:417–429.
32. Atilgan, A. R., S. R. Durell, …, I. Bahar. 2001. Anisotropy of fluctuation dynamics of proteins with an elastic network model. *Biophys. J.* 80:505–515.
33. Tama, F., and Y. H. Sanejouand. 2001. Conformational change of proteins arising from normal mode calculations. *Protein Eng.* 14:1–6.
34. Bahar, I., T. R. Lezon, …, E. Eyal. 2010. Global dynamics of proteins: bridging between structure and function. *Annu. Rev. Biophys.* 39:23–42.
35. Mahajan, S., and Y.-H. Sanejouand. 2015. On the relationship between low-frequency normal modes and the large-scale conformational changes of proteins. *Arch. Biochem. Biophys.* 567:59–65.
36. Eyal, E., G. Lum, and I. Bahar. 2015. The anisotropic network model web server at 2015 (ANM 2.0). *Bioinformatics.* 31:1487–1489.
37. Li, H., Y.-Y. Chang, …, I. Bahar. 2016. iGNM 2.0: the Gaussian network model database for biomolecular structural dynamics. *Nucleic Acids Res.* 44:D415–D422.
38. Bakan, A., and I. Bahar. 2009. The intrinsic dynamics of enzymes plays a dominant role in determining the structural changes induced upon inhibitor binding. *Proc. Natl. Acad. Sci. USA.* 106:14349–14354.
39. Meireles, L., M. Gur, …, I. Bahar. 2011. Pre-existing soft modes of motion uniquely defined by native contact topology facilitate ligand binding to proteins. *Protein Sci.* 20:1645–1658.
40. Yang, L., G. Song, …, R. L. Jernigan. 2008. Close correspondence between the motions from principal component analysis of multiple HIV-1 protease structures and elastic network modes. *Structure.* 16:321–330.
41. Kurkcuoglu, Z., I. Bahar, and P. Doruker. 2016. ClustENM: ENM-based sampling of essential conformational space at full atomic resolution. *J. Chem. Theory Comput.* 12:4549–4562.
42. Kandzia, F., K. Ostermeir, and M. Zacharias. 2019. Global dynamics of yeast Hsp90 middle and C-terminal dimer studied by advanced sampling simulations. *Front. Mol. Biosci.* 6:93.
43. Sankar, K., S. K. Mishra, and R. L. Jernigan. 2018. Comparisons of protein dynamics from experimental structure ensembles, molecular dynamics ensembles, and coarse-grained elastic network models. *J. Phys. Chem. B.* 122:5409–5417.
44. Leioatts, N., T. D. Romo, and A. Grossfield. 2012. Elastic network models are robust to variations in formalism. *J. Chem. Theory Comput.* 8:2424–2434.
45. Fuglebakk, E., S. P. Tiwari, and N. Reuter. 2015. Comparing the intrinsic dynamics of multiple protein structures using elastic network models. *Biochim. Biophys. Acta.* 1850:911–922.
46. Kantarci, N., P. Doruker, and T. Haliloglu. 2006. Cooperative fluctuations point to the dimerization interface of p53 core domain. *Biophys. J.* 91:421–432.
47. Wang, B., J. Weng, …, W. Wang. 2011. Elastic network model-based normal mode analysis reveals the conformational couplings in the tripartite AcrAB-TolC multidrug efflux complex. *Proteins.* 79:2936–2945.
48. Marcos, E., R. Crehuet, and I. Bahar. 2011. Changes in dynamics upon oligomerization regulate substrate binding and allostery in amino acid kinase family members. *PLoS Comput. Biol.* 7:e1002201.
49. Li, H., N. Sharma, …, I. Bahar. 2017. Dynamic modulation of binding affinity as a mechanism for regulating interferon signaling. *J. Mol. Biol.* 429:2571–2589.
50. Katebi, A. R., and R. L. Jernigan. 2015. Aldolases utilize different oligomeric states to preserve their functional dynamics. *Biochemistry.* 54:3543–3554.
51. Simonson, T., and D. Perahia. 1992. Normal modes of symmetric protein assemblies. Application to the tobacco mosaic virus protein disk. *Biophys. J.* 61:410–427.
52. Oakley, A. J., P. Prosselkov, …, N. E. Dixon. 2003. Flexibility revealed by the 1.85 A crystal structure of the beta sliding-clamp subunit of *Escherichia coli* DNA polymerase III. *Acta Crystallogr. D Biol. Crystallogr.* 59:1192–1199.
53. Fernandez-Leiro, R., J. Conrad, …, M. H. Lamers. 2015. cryo-EM structures of the *E. coli* replicative DNA polymerase reveal its dynamic interactions with the DNA sliding clamp, exonuclease and τ. *eLife.* 4:e11134.
54. Kelch, B. A., D. L. Makino, …, J. Kuriyan. 2011. How a DNA polymerase clamp loader opens a sliding clamp. *Science.* 334:1675–1680.
55. Antson, A. A., E. J. Dodson, …, P. Gollnick. 1999. Structure of the Trp RNA-binding attenuation protein, TRAP, bound to RNA. *Nature.* 401:235–242.
56. Bahar, I., and A. J. Rader. 2005. Coarse-grained normal mode analysis in structural biology. *Curr. Opin. Struct. Biol.* 15:586–592.
57. Bahar, I., T. R. Lezon, …, I. H. Shrivastava. 2010. Normal mode analysis of biomolecular structures: functional mechanisms of membrane proteins. *Chem. Rev.* 110:1463–1497.
58. Yang, L.-W., A. J. Rader, …, I. Bahar. 2006. oGNM: online computation of structural dynamics using the Gaussian network model. *Nucleic Acids Res.* 34:W24–W31.
59. Li, H., Y.-Y. Chang, …, L.-W. Yang. 2017. DynOmics: dynamics of structural proteome and beyond. *Nucleic Acids Res.* 45:W374–W380.
60. Jernigan, R., G. Raghunathan, and I. Bahar. 1994. Characterization of interactions and metal ion binding sites in proteins. *Curr. Opin. Struct. Biol.* 4:256–263.
61. Bakan, A., L. M. Meireles, and I. Bahar. 2011. ProDy: protein dynamics inferred from theory and experiments. *Bioinformatics.* 27:1575–1577.
62. Ming, D., and M. E. Wall. 2005. Allostery in a coarse-grained model of protein dynamics. *Phys. Rev. Lett.* 95:198103.
63. Zheng, W., and B. R. Brooks. 2005. Probing the local dynamics of nucleotide-binding pocket coupled to the global dynamics: myosin versus kinesin. *Biophys. J.* 89:167–178.
64. Eyal, E., and I. Bahar. 2008. Toward a molecular understanding of the anisotropic response of proteins to external forces: insights from elastic network models. *Biophys. J.* 94:3424–3435.

65. Schrödinger, LLC. 2019. The PyMOL Molecular Graphics System, Version 2.3. Schrödinger, LLC, New York.

66. Best, R. B., X. Zhu, …, A. D. Mackerell, Jr. 2012. Optimization of the additive CHARMM all-atom protein force field targeting improved sampling of the backbone φ, ψ and side-chain χ(1) and χ(2) dihedral angles. *J. Chem. Theory Comput.* 8:3257–3273.

67. Hunter, J. D. 2007. Matplotlib: a 2D graphics environment. *Comput. Sci. Eng.* 9:90–95.

68. Heltzel, J. M. H., S. K. Scouten Ponticelli, …, M. D. Sutton. 2009. Sliding clamp-DNA interactions are required for viability and contribute to DNA polymerase management in *Escherichia coli*. *J. Mol. Biol.* 387:74–91.

69. Blainey, P. C., G. Luo, …, X. S. Xie. 2009. Nonspecifically bound proteins spin while diffusing along DNA. *Nat. Struct. Mol. Biol.* 16:1224–1229.

70. Kochaniak, A. B., S. Habuchi, …, A. M. van Oijen. 2009. Proliferating cell nuclear antigen uses two distinct modes to move along DNA. *J. Biol. Chem.* 284:17700–17710.

71. Bowman, G. D., M. O'Donnell, and J. Kuriyan. 2004. Structural analysis of a eukaryotic sliding DNA clamp-clamp loader complex. *Nature.* 429:724–730.

72. Kazmirski, S. L., Y. Zhao, …, J. Kuriyan. 2005. Out-of-plane motions in open sliding clamps: molecular dynamics simulations of eukaryotic and archaeal proliferating cell nuclear antigen. *Proc. Natl. Acad. Sci. USA.* 102:13801–13806.

73. Adelman, J. L., J. D. Chodera, …, D. Barsky. 2010. The mechanical properties of PCNA: implications for the loading and function of a DNA sliding clamp. *Biophys. J.* 98:3062–3069.

74. Alley, S. C., V. K. Shier, …, S. J. Benkovic. 1999. Sliding clamp of the bacteriophage T4 polymerase has open and closed subunit interfaces in solution. *Biochemistry.* 38:7696–7709.

75. Zou, T., V. A. Risso, …, S. B. Ozkan. 2015. Evolution of conformational dynamics determines the conversion of a promiscuous generalist into a specialist enzyme. *Mol. Biol. Evol.* 32:132–143.

76. Haliloglu, T., and I. Bahar. 2015. Adaptability of protein structures to enable functional interactions and evolutionary implications. *Curr. Opin. Struct. Biol.* 35:17–23.

77. Douma, L. G., K. K. Yu, …, L. B. Bloom. 2017. Mechanism of opening a sliding clamp. *Nucleic Acids Res.* 45:10178–10189.

78. Bhattacharyya, M., M. M. Stratton, …, J. Kuriyan. 2016. Molecular mechanism of activation-triggered subunit exchange in $Ca^{(2+)}$/calmodulin-dependent protein kinase II. *eLife.* 5:e13405.

79. Yewdall, N. A., T. M. Allison, …, J. A. Gerrard. 2018. Self-assembly of toroidal proteins explored using native mass spectrometry. *Chem. Sci. (Camb.).* 9:6099–6106.

80. Malay, A. D., N. Miyazaki, …, J. G. Heddle. 2019. An ultra-stable gold-coordinated protein cage displaying reversible assembly. *Nature.* 569:438–442.